The Manifestation of Spatial Wideband Effect in Circular Array: From Beam Split to Beam Defocus

Zidong Wu and Linglong Dai, *Fellow, IEEE*

***Abstract*—Millimeter-wave (mmWave) and terahertz (THz) communications with hybrid precoding architectures have been regarded as energy-efficient solutions to fulfill the vision of high-speed transmissions for 6G communications. Benefiting from the advantages of providing a wide scan-range and flat array gain, the uniform circular array (UCA) has attracted much attention. However, the growing bandwidth of mmWave and THz communications require frequency-dependent phase shifts, which can not be perfectly realized through frequency-independent phase shifters (PSs) in classical hybrid precoding architectures. This mismatch causes the beam defocus effect in UCA wideband communications, where high-gain beams could not form at non-central frequencies in any direction. In this paper, we first investigate the characteristics of the beam defocus effect distinguishing itself from the beam split effect in uniform linear array (ULA) systems. The beamforming gain in both frequency domain and angular domain is analyzed, characterizing the beamforming loss caused by the beam defocus effect. Then, the delay-phase precoding (DPP) architecture leveraging true-time-delays (TTDs) to generate frequency-dependent phase shifts is employed to mitigate the beam defocus effect. Finally, performance analysis and extensive simulation results are provided to evaluate the effectiveness of DPP architecture in UCA systems.**

***Index Terms*—Massive MIMO, mmWave communications, uniform circular array (UCA), hybrid precoding, beam defocus.**

I. Introduction

To meet the ever-increasing growth of data transmission demand, high-frequency bands such as millimeter-wave (mmWave) and terahertz (THz) are promising to provide abundant spectrum resources for future sixth-generation (6G) communications. Nevertheless, high-frequency communications have to face the challenge of severe propagation attenuation, which dramatically limits the coverage area of wireless communications. To combat the high propagation attenuation, massive multiple-input multiple-output (MIMO) plays a key role in forming high-gain directional beams to increase the received signal power, which significantly extends the communication distances [1].

In massive MIMO systems, the energy-efficient hybrid precoding architecture has been widely adopted in existing 5G communications to generate high-gain beams at bearable power consumption. Compared with conventional digital precoding schemes, hybrid precoding avoids employing a large number of power-consuming radio frequency (RF) chains by dividing a large-dimension digital precoder into a small-dimension digital precoder with RF chains and a large-dimension analog precoder implemented by phase shifters (PSs) [2], [3]. Due to the hardware constraint of analog PSs, additional constraints are imposed in analog precoding designs, increasing the difficulty in designing hybrid precoding in mmWave and THz communications [4], [5].

A. Prior Works

Enormous works have investigated hybrid precoding methods in both narrowband and wideband systems. In narrowband mmWave communication systems, the initial work in [5] proposed a compressed sensing (CS)-based precoding method, where an orthogonal matching pursuit (OMP) method was employed to capture the channel sparsity in the angular domain to determine the analog precoder. To further improve the system spectrum efficiency, an iterative optimization method based on the Riemannian manifold is proposed in [6] to optimize the analog precoders. Nevertheless, the above-mentioned works assumed a fully-connected hybrid precoding network, where each RF chain connected to all antennas via PSs. The fully-connected architecture still introduced overwhelming hardware complexity. To solve this problem, the sub-connected architecture where each RF is only connected to a subset of antennas was proposed in [7]. The successive interference cancellation (SIC) method was employed to derive closed-form digital and analog precoders. Moreover, a dynamic array-of-subarray architecture was further proposed, where the connections between PSs and RF chains can be dynamically adjusted to adapt to different channel conditions in a sub-connected manner [4].

Although the above methods work well for narrowband communications, the hybrid precoding design experiences serious challenges in wideband mmWave communications [8]. Most existing works in wideband hybrid precoding designs rely on the PS network to adjust signal phase shifts at different antennas to form constructive interference in desired directions. In wideband communications, the required phase shifts to form constructive interference are frequency-dependent. Unfortunately, PSs could only generate the same phase shifts at different frequencies, which is called frequency-independent. This mismatch results in that PSs could only generate desired phase shifts at the central frequency [9], failing to generate required phase shifts at non-central frequencies. This phenomenon is also termed the spatial wideband effect [10], [11].

This work was supported in part by the National Natural Science Foundation of China under Grant 62031019 and in part by the European Commission through the H2020-MSCA-ITN META WIRELESS Research Project under Grant 956256. An earlier version of this paper was presented in part at the IEEE Global Communications Conference (GLOBECOM 2023). *(Corresponding author: Linglong Dai.)*

The authors are with the Department of Electronic Engineering, Tsinghua University, Beijing 100084, China, and also with the Beijing National Research Center for Information Science and Technology (BNRist), Beijing 100084, China (e-mails: wuzd19@mails.tsinghua.edu.cn, daill@tsinghua.edu.cn).

As a result, at non-central frequencies the beams are squinted from the desired direction in uniform linear array (ULA) systems, resulting in severe beamforming loss [12], [13]. This effect was termed the *beam squint* effect in mmWave and became more significant in THz communications, which was identified as the *beam split* effect. For illustration simplicity, in this paper, we unify these names as the *beam split* effect.

Existing works that were able to mitigate the beam split effect could be classified into two categories, i.e. from the perspective of algorithm design and from the perspective of architecture design. In works on algorithm designs, the hybrid precoding algorithm is elaborately designed to mitigate the beam split effect while the hardware architecture remains the same as classical hybrid precoding. A frequency-selective hybrid precoding algorithm was proposed in [14], where the analog precoder was exhaustively searched from a quantized codebook to maximize the achievable rate. The method employing the channel covariance matrix over the wide bandwidth to efficiently design the analog precoder was proposed in [15]. Nevertheless, although the methods above could alleviate the beam split effect by treating it as frequency-selective factors, the pattern of beam split effect was not explicitly considered in algorithm design. It was revealed that the beam split effect would result in channels at different frequencies possessing different subspaces [16]. By considering all subspaces at different frequencies, a common analog precoding matrix for all subcarriers could be constructed to achieve a balanced performance in single-user MIMO communications. While in multi-user MIMO communications, an additional phase compensation operation was carried out to alleviate the beam split effect [17]. Moreover, the wide beams were also leveraged to combat the beam split effect in [18].

In the second architecture design method, true-time-delay (TTD) devices have been noticed to address the beam split effect for its capability of generating frequency-dependent phase shifts. A fully-linked TTD architecture where each antenna was fed by a separate TTD was proposed to generate frequency-dependent beamsteering in radar systems [19], [20]. For phased array communications, a low-complexity TTD-based subarray architecture was proposed to maintain a desired wavefront in the wide bandwidth to enable wideband scanning [21]. In this architecture, the array is classified into different subarrays, where one TTD is inserted behind each subarray and phase shifters are connected to each antenna. Inspired by this architecture, a delay-phase precoding (DPP) scheme was proposed to mitigate the beam split effect in THz communications, where PSs and TTDs are combined to generate desired frequency-dependent phase shifts [22]. Moreover, a fixed TTD network was developed in [9] to avoid the employment of complicated adjustable TTDs.

Existing works in wideband hybrid precoding designs mainly focused on the deployment of ULA. Nevertheless, since the effective array aperture of ULA dramatically reduces near the edges of ULA, the beampattern is severely distorted at large incident or departure angles [23]. To overcome this drawback, the uniform circular array (UCA) has been regarded as a feasible solution to provide a wide scan-range and invariant beampattern along the entire 360° azimuth plane [24]. Owing to its capability of maintaining uniform beampatterns, UCA has gained much attention in mmWave communications to improve the system performance. To be specific, it was revealed that compared with the 1D deployment of ULA, a higher number of antennas could be deployed at a limited space with the 2D form of UCA, providing higher antenna gain to overcome the propagation attenuation in mmWave communications [25]. Benefiting from the uniform beampattern of UCA, it has been proved that UCA outperformed ULA and uniform planar array (UPA) counterparts by improving the ergodic capacity and achievable spectrum efficiency [26], [27]. Later in [28], UCA was leveraged to improve the bit error rate (BER) performance compared with ULA implementations.

In UCA communication systems, beamforming techniques have been investigated in narrowband systems [29]–[34] and wideband digital precoding systems [35]–[38]. In the early work [29], the steering vectors, scan-angle range, and array directivity of UCA were thoroughly investigated. The beamwidth and array directivity with respect to the number of antennas were further analyzed, indicating that arbitrarily narrow beamwidth could be achieved to benefit from the spatial multiplexing gain in massive MIMO systems [30]. A hybrid beamforming scheme with UCA for multi-user communications was developed in [31], where a phase-mode transformation with infinite-resolution PSs was proposed to obtain the Vandermonde structure of steering vectors like in ULA systems. A hybrid precoding scheme with low-resolution PSs and digital-to-analog converters (DACs) was further investigated for UCA and other 2D arrays [32]. The narrowband beamforming with UCA for security communications and maritime communications were also investigated in [33] and [34], respectively. Nevertheless, the aforementioned beamforming techniques on narrowband UCA systems failed to adapt to the wideband conditions, since the beamforming vectors were only calculated at the central frequency and could not obtain optimal beamforming gain over the wide bandwidth [39]. To enable wideband communications with UCA, the frequency invariant beamformer (FIB) was proposed in [35], aiming to efficiently develop digital beamformers with the phase mode to generate high beamforming gain invariant with frequencies. This method was further generalized into wideband UCA channel estimations [36], channel characterizations [37], and source localizations in microphone arrays [38].

However, the aforementioned works on UCA rarely consider the energy-efficient hybrid precoding architecture for wideband communications. The hybrid precoding scheme with UCA will also introduce the spatial wideband effect, i.e. the mismatch of frequency-independent phase shifts of PSs and required frequency-dependent phase shifts to perform beamforming. The existing analysis of the spatial wideband effect was restricted to ULA systems, failing to characterize the beamforming gain performance and beam pattern in UCA systems. In this paper, we reveal that due to the variation of the array geometry, the spatial wideband effect will have a new manifestation different from the beam split effect, which brings severe beamforming loss in wideband UCA communications. To the best of our knowledge, such a phenomenon in UCA systems has not been investigated in existing research,

let alone the solutions to alleviate this effect.

B. Our Contributions

In this paper, we first reveal the manifestation of the spatial wideband effect in UCA systems as the *beam defocus* effect[1], and characterize the beamforming loss resulting from the effect in UCA systems. Then, the DPP architecture incorporating TTDs is proposed to alleviate the beam defocus effect. The contributions of the paper are listed as follows.

- We first reveal that the spatial wideband effect is highly dependent on the array geometry and its manifestation in circular arrays is the beam defocus effect. Different from the beam split effect for ULA where beams are directed to different directions at different frequencies, high-gain beams could no longer form at non-central frequencies in the same plane of UCA. Despite the similar root cause, this effect is termed the beam defocus effect to highlight its distinct beampatterns in the 2D space different from the beam split effect.
- The mechanism of the beam defocus effect is investigated, where the 2D array pattern in both the frequency and angular domains is characterized. We first reveal that the beamforming gain in the frequency domain could be approximated with the zero-order Bessel function, indicating a severe beamforming loss in wideband UCA communications with hybrid precoding architectures. Then, the beam pattern in the angular domain between beam defocus effect and beam split effect is compared, revealing the distinguishing features of beam defocus effect.
- To mitigate the beam defocus effect, the DPP architecture is employed in UCA mmWave wideband communications. Inspired by the method of applying DPP to mitigate the beam split effect in ULA systems, the feasibility of employing DPP to mitigate the beam defocus effect is explored. By inserting a TTD before each subarray that connects to multiple PSs, the required frequency-dependent phase shifts could be generated with the aid of both TTDs and PSs to overcome the beam defocus effect. The corresponding DPP algorithm for designing the TTDs and PSs is provided. It is also revealed that the key idea for designing time delays is to compensate for the mismatch of frequency-independent and frequency-independent phase shifts at the center of each subarray. The performance of DPP is characterized in closed form, providing performance guarantees for the DPP architecture. Finally, simulation results are provided to verify the effectiveness of the proposed DPP methods.

C. Organization and Notation

Organization: The remainder of the paper is organized as follows. Section II introduces the wideband UCA communication system model. Section III investigates the beam defocus effect in both frequency and angular domains. The DPP architecture is employed to alleviate the beam defocus effect in Section IV. The performance analysis is provided in Section V. Simulation results are provided in Section VI, and conclusions are drawn in Section VII.

Notations: Lower-case and upper-case boldface letters represent vectors and matrices, respectively; $\mathbb{C}$ denotes the set of complex numbers; $[\cdot]^{-1}$, $[\cdot]^T$ and $[\cdot]^H$ denote the inverse, transpose and conjugate-transpose, respectively; $[\mathbf{A}]_{i,j}$ denotes the i^{th} row and j^{th} column of matrix $\mathbf{A}$; $\text{blkdiag}(\mathbf{A})$ denotes a block diagonal matrix consisting of the columns of $\mathbf{A}$; $\mathcal{CN}(\mu, \sigma^2)$ denotes the complex Gaussian distribution with mean μ and variance σ^2.

II. System Model

We first consider a downlink massive MIMO mmWave wideband system, where the classical hybrid precoding scheme is adopted. The base station (BS) is equipped with an N-element UCA while the user is assumed to be equipped with an N_{r}-element ULA. The BS employs N_{RF} RF chains, each of which connects to all antennas in a fully-connected manner [5]. To harvest the spatial multiplexing gain, N_{s} data streams are multiplexed, satisfying $N_{\text{s}} \leq N_{\text{RF}} \leq N$. We assume $N_{\text{s}} = N_{\text{RF}} \ll N$ in this paper for illustration simplicity. The OFDM model with M subcarriers is employed and the bandwidth is set to B. The central frequency is denoted by f_c and frequency of the m^{th} subcarrier is denoted by $f_m = f_c + \frac{B(2m-1-M)}{2M}$. Thus, the received signal at user on the m^{th} subcarrier $\mathbf{y}_m \in \mathbb{C}^{N_{\text{r}} \times 1}$ could be expressed as

$$\mathbf{y}_m = \rho \mathbf{H}_m^H \mathbf{F}_{\text{A}} \mathbf{F}_{\text{D},m} \mathbf{s}_m + \mathbf{n}_m, \tag{1}$$

where $\mathbf{H}_m \in \mathbb{C}^{N \times N_{\text{r}}}$ denotes the channel, $\mathbf{F}_{\text{A}} \in \mathbb{C}^{N \times N_{\text{RF}}}$ and $\mathbf{F}_{\text{D},m} \in \mathbb{C}^{N_{\text{RF}} \times N_{\text{s}}}$ denote the analog precoder and digital precoder, respectively. Note that since the digital precoder is conducted before digital-to-analog converters (DACs), it could be performed subcarrier by subcarrier and therefore is frequency-dependent. On the contrary, the analog precoder implemented by PSs introduces frequency-invariant phase shifts at different frequencies. Thus, $\mathbf{F}_{\text{A}}$ is frequency-independent. Due to the circuit restrictions, the analog precoder is constant-modulus constrained with $|[\mathbf{F}_{\text{A}}]_{i,j}| = \frac{1}{\sqrt{N}}$. The transmitted signal $\mathbf{s}_m \in \mathbb{C}^{N_{\text{s}} \times 1}$ and noise $\mathbf{n}_m \in \mathbb{C}^{N_{\text{r}} \times 1}$ follow $\mathbb{E}(\mathbf{s}_m \mathbf{s}_m^H) = \frac{1}{N_{\text{s}}} \mathbf{I}_{N_{\text{s}}}$ and $\mathbf{n}_m \sim \mathcal{CN}(0, \sigma_n^2)$, respectively.

Adopting the widely-adopted multi-path model [5], [40], the channel at the m^{th} subcarrier could be written as

$$\mathbf{H}_m = \sqrt{\frac{N}{L}} \sum_{l=1}^{L} g_l e^{-j2\pi\tau_l f_m} \mathbf{a}_m(\phi_l) \bar{\mathbf{a}}_m(\varphi_l)^H, \tag{2}$$

where $\mathbf{a}_m(\cdot)$ and $\bar{\mathbf{a}}_m(\cdot)$ denote the beam steering vectors at the BS side and user side, respectively. The number of resolvable paths is set to L. Notation g_l, τ_l, ϕ_l and φ_l denote the complex gain, delay, angle of departure (AoD), and angle of arrival (AoA) of the l^{th} path, respectively. The beam steering vector can be viewed as a frequency response vector for an impinging wave, which is highly dependent on the array structure. In this paper, UCA is employed at BS shown in Fig. 1. Thus, the beam steering vector corresponding to the physical direction ϕ can be written as [29]

$$\mathbf{a}_m(\phi) = \frac{1}{\sqrt{N}} \left[e^{j\eta_m \cos(\phi - \psi_0)}, \cdots, e^{j\eta_m \cos(\phi - \psi_{N-1})} \right]^T, \tag{3}$$

[1]Simulation codes are provided to reproduce the results presented in this article: http://oa.ee.tsinghua.edu.cn/dailinglong/publications/publications.html.

This article has been accepted for publication in IEEE Transactions on Communications. This is the author's version which has not been fully edited and content may change prior to final publication. Citation information: DOI 10.1109/TCOMM.2024.3354199

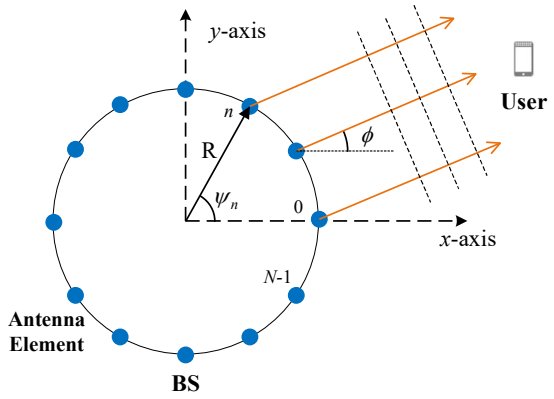

Fig. 1. The geometry of UCA at BS.

where $\eta_m = \frac{2\pi R}{c} f_m$ for $m = 1, 2, \cdots, M$ and $\psi_n = \frac{2\pi n}{N}$ for $n = 0, 1, \cdots, N-1$. Since there are more strict requirements on the array deployment on the user side, we assume that ULA is employed by users. Thus, the steering vector at the receiver could be expressed as

$$\bar{\mathbf{a}}_m(\varphi) = \frac{1}{\sqrt{N_r}} \left[1, e^{j\frac{2\pi d f_m}{c}\sin\varphi}, \cdots, e^{j\frac{2\pi(N_r-1)df_m}{c}\sin\varphi}\right]^T. \tag{4}$$

It is worth noting that the beam steering vectors for constructing the channel are frequency-dependent, which means the phase differences between different antennas change with the frequency. This phenomenon is inconspicuous in narrowband systems, since the phase shift in the beam steering vector only varies with the frequency in a limited range. However, the varying range of the phases is significantly extended in wideband systems, which causes the problem of non-ideal beamforming gain in hybrid precoding architectures [22]. This effect will be discussed in detail in the following section.

III. Beam Defocus Effect in UCA Systems

In this section, the mechanism of the beam defocus effect in wideband UCA systems will be first introduced. Then, the beamforming gain pattern of UCA in both frequency and angular domains caused by the beam defocus effect is analyzed, characterizing the beamforming loss resulting from beam defocus effect.

In hybrid precoding architectures, the analog precoder and digital precoder are combined to generate directional beams to obtain the spatial multiplexing gain and beamforming gain [1]. Specifically, the analog precoding is aiming to form high-gain beams by performing constructive interference in desired directions. To achieve this goal, the PSs are elaborately designed to compensate for the phase differences between different antennas to form equal-phase planes perpendicular to the desired direction. However, it has been revealed that PSs could only generate frequency-independent phase shifts [22]. On the contrary, to performing constructive interference in the same direction, the required phase shifts are frequency-dependent in wideband communications, which has also been reflected in (3) and (4). This mismatch of the frequency-independent phase shifts generated by PSs and the required frequency-dependent phase shifts is often termed the spatial wideband effect [10].

Recently, it has been revealed that the spatial wideband effect has given rise to the beam split effect in ULA systems [22], which can be viewed as a manifestation of the spatial wideband effect corresponding to the linear array geometry. Nevertheless, the beam pattern analysis of the beam split effect in [22] is only feasible in ULA systems. As the array geometry varies from linear to circular, the spatial wideband effect will be embodied as another manifestation, which shall be discussed as follows.

Lemma 1. If the frequency-independent beam steering vector $\mathbf{a}_c(\phi_0)$ is employed, the achieved beamforming gain at the subcarrier f_m in the desired direction ϕ_0 could be expressed as

$$\begin{aligned} G_m(\mathbf{a}_c(\phi_0), \phi_0) &= \left|\mathbf{a}_m^H(\phi_0)\mathbf{a}_c(\phi_0)\right| \\ &\approx \left|J_0(\eta_m - \eta_c)\right| = \left|J_0\left(\frac{2\pi R(f_m - f_c)}{c}\right)\right|, \end{aligned} \tag{5}$$

where $\eta_m = \frac{2\pi R}{c} f_m$, $\eta_c = \frac{2\pi R}{c} f_c$ and $J_0(\cdot)$ denotes the zero-order Bessel function of the first kind.

Proof. When assuming a large number of elements N, the summation operator in (5) could be approximated with the integral operator, written as

$$\begin{aligned} G_m(\mathbf{a}_c(\phi_0), \phi_0) &= \left|\frac{1}{N}\sum_{n=0}^{N-1} e^{-j(\eta_m - \eta_c)\cos(\phi_0 - \psi_n)}\right| \\ &\approx \left|\frac{1}{2\pi}\int_0^{2\pi} e^{-j(\eta_m - \eta_c)\cos(\phi_0 - x)}\mathrm{d}x\right| \\ &\overset{(a)}{=} \left|J_0(\eta_m - \eta_c)\right| = \left|J_0\left(\frac{2\pi R(f_m - f_c)}{c}\right)\right|, \end{aligned} \tag{6}$$

where equation (a) is derived from the definition of the zero-order Bessel function of the first kind [41]. This completes the proof. Another proof method directly addressing the summation operator can be found in [42]. ■

Remark 1. Lemma 1. has characterized the beamforming loss resulting from the spatial wideband effect in the frequency domain. According to the property of $J_0(x)$, the beamforming gain employing PSs could only achieve its maximum when $f_m = f_c$, i.e. at the central frequency. The perfect constructive interference could not form at any subcarrier other than the central frequency, introducing unwilling beamforming loss across the wide bandwidth. In addition, the beamforming gain is not dependent on the angle ϕ, which results from the rotational symmetry of UCA. This is also one of the distinguishing features of UCAs.

The normalized beamforming gain at different frequencies is plotted in Fig. 2. The central frequency is set to 30 GHz with the bandwidth $B = 3$ GHz. The BS is equipped with a 256-element half-wavelength spaced UCA. It is shown that the optimal beamforming could only be achieved at the central frequency, which is consistent with the analysis in **Lemma 1**. According to the overall downtrend of $|J_0(x)|$, a larger frequency deviation from the central frequency will result in a more severe beamforming loss. In addition, the destructive

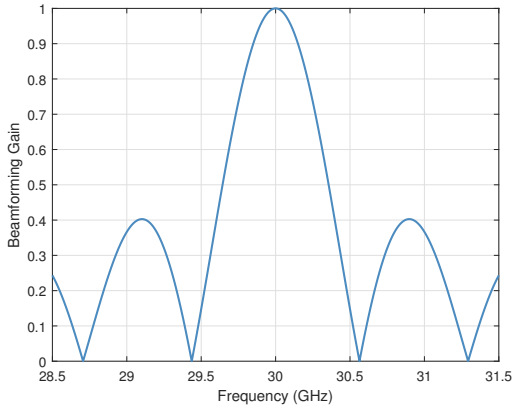

Fig. 2. The beamforming gain achieved with frequency-independent phase shifts at different frequencies.

interference could even be formed at certain frequencies, resulting in zero beamforming gain.

The analysis above has revealed that wideband communications using UCA will experience significant beamforming loss due to constraints imposed by frequency-independent PSs in hybrid precoding. This phenomenon bears a resemblance to the beam split effect observed in ULA. In the following lemma, we will elucidate the distinctive characteristics of the beam defocus effect as distinguished from the beam split effect.

Lemma 2. If the frequency-independent beam steering vector $\mathbf{a}_c(\phi_0)$ is employed, the achieved beamforming gain at frequency f_m at any direction ϕ could be expressed as

$$G_m(\mathbf{a}_c(\phi_0), \phi) = \left|\mathbf{a}_m^H(\phi)\mathbf{a}_c(\phi_0)\right| \approx \left|J_0(\xi)\right|, \tag{7}$$

where the parameter ξ is defined as

$$\xi = \sqrt{\eta_m^2 + \eta_c^2 - 2\eta_m\eta_c\cos(\phi - \phi_0)}. \tag{8}$$

Proof. The proof is provided in Appendix A. ■

This lemma characterizes the beam pattern of the beam defocus effect in the angular domain. According to the property of $J_0(\cdot)$, the beamforming gain could only achieve the maximum when $\xi = 0$, i.e. $f_m = f_c$ and $\phi = \phi_0$ are simultaneously satisfied. Note that if $\phi = \phi_0$ is satisfied, the result in **Lemma 2** will degrade into **Lemma 1**. Therefore, **Lemma 2** depicts a more general case where ϕ can be arbitrarily selected. For fixed $f_m \neq f_c$, the normalized beamforming gain at f_m could not reach 1 at any azimuth angle. As a consequence, high-gain beams with optimal beamforming gain could not form except at the central frequency. This phenomenon is different from the beam split effect for ULA systems, where the high-gain beams with optimal gain split into a specific physical direction at different frequencies.

To clearly exhibit the differences between beam defocus effect beam split effect, a comparison of the beam pattern in the angular domain is shown in Fig. 3, where different colored lines represent the beam pattern at different frequencies. Specifically, the high-gain beams slightly squint from the desired direction but retain the same beam pattern in the beam split effect, as shown in Fig. 3(a). On the contrary, the beam pattern is severely distorted at non-central frequencies in

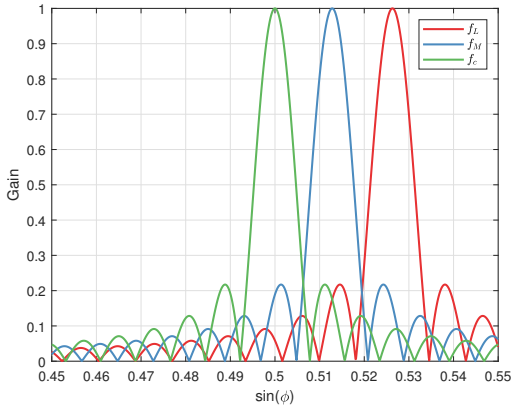

(a) Beam Split Effect

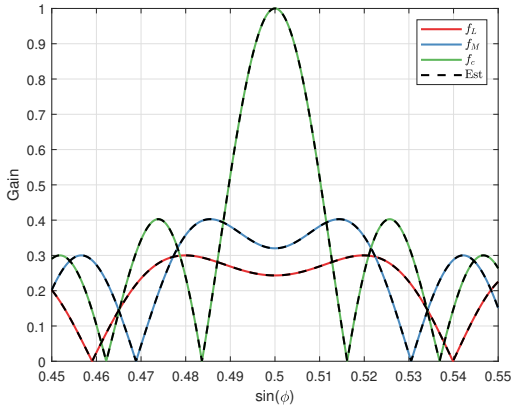

(b) Beam Defocus Effect

Fig. 3. Comparison over the beam split effect and beam defocus effect in the angular domain. Both systems are designed to generate beams towards $\sin(\phi) = 0.5$ at the central frequency. $f_L = 28.5$ GHz and $f_c = 30$ GHz denote the lowest frequency and central frequency while f_M denotes the middle point as $f_M = \frac{f_L + f_c}{2}$.

the beam defocus effect, as shown in Fig. 3(b). The high-gain beams no longer exist in the azimuth plane, which is consistent with the result in **Lemma 2**. Since this effect is similar to the defocus phenomenon in photography where the photo becomes blurred due to failed focusing, we name it the *beam defocus effect* due to the failure in compensating the phases at different frequencies. In addition, the colored solid lines in Fig. 3(b) denote the accurately calculated beamforming gain across the bandwidth while the black dashed lines denote the estimated beamforming gain with **Lemma 2**. The consistency between the solid and dashed lines suggests that the estimation presented in equation (7) can achieve a high level of accuracy.

Remark 2. It is worth noting that the beam defocus effect could be viewed as a special case of the beam split effect. For the similarities, the root cause of both effects is the mismatch between the generated frequency-independent phase shifts and the required frequency-dependent phase shifts. In addition, when relaxing the 2D space restriction into 3D space, it can be found that the original high-gain beam will split into two beams toward different *elevation angles* at the higher half frequency band. However, the beam defocus effect also possesses some distinct features. First, no high gain beams

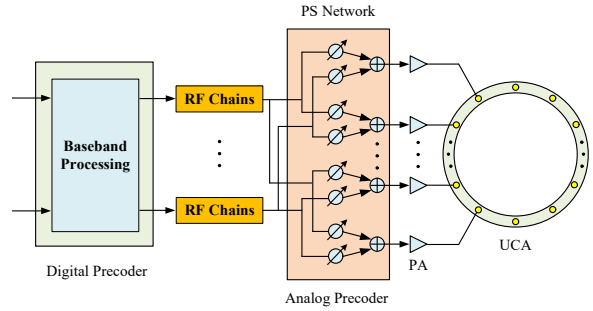

(a) Classical Hybrid Precoding Architecture

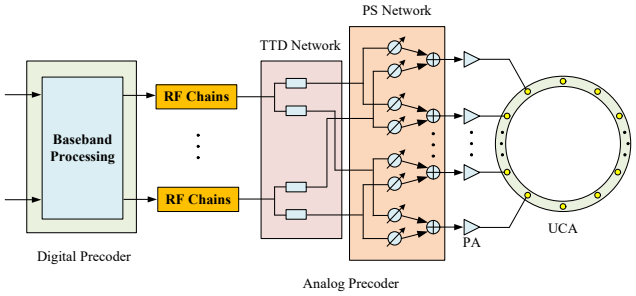

(b) Delay-Phase Precoding Architecture

Fig. 4. Comparison of the classical hybrid precoding architecture and employed DPP architecture.

could be observed by users which are assumed to be in the same plane of UCA. Only the distorted beams are presented as shown in Fig. 3(b). Second, no high-gain beams could be observed in any direction in the whole 3D space at the lower half frequency band, which seldom occurs in ULA systems[2]. Therefore, this effect in UCA systems is named the beam defocus effect to highlight its distinct features in the 2D space compared with the classical beam split effect.

IV. DPP Architecture to Alleviate the Beam Defocus Effect

To retrieve the beamforming loss resulting from the beam defocus effect, the DPP architecture is employed in this section. The precoding algorithm will also be provided and the beamforming gain with DPP methods will be investigated.

A. DPP Architecture

As discussed in previous sections, severe beamforming loss will be introduced in classical PS-based hybrid precoding architectures due to the beam defocus effect, which remarkably worsens the received signal quality in the whole bandwidth. As a result, the wideband UCA communications will suffer from serious performance loss in hybrid precoding architectures.

To break the hardware constraints of PS that could only generate frequency-independent phase shifts, TTDs have been inserted before PSs [9], [22]. In this architecture, the delay of TTDs and the phase shifts of PSs are combined to produce frequency-dependent phase shifts to cope with the beam split effect in ULA, which is also termed the DPP architecture.

[2]We assume that the user is confined to the same plane of UCA to benefit from UCA's advantage of providing uniform beampatterns in the azimuth plane in this paper. Thus, the analysis of 3D beamforming is beyond the scope of this paper and thereby could not be illustrated in detail here.

It is noteworthy that the beam split effect and beam defocus effect, despite their distinct manifestations, stem from the same underlying cause, the mismatch between the generated frequency-independent phase shifts and the required frequency-dependent phase shifts. Drawing inspiration from this discovery, we propose to generalize the DPP architecture originally employed in ULA systems into UCA systems to mitigate the beam defocus effect. In contrast to the classical hybrid precoding architecture depicted in Fig. 4(a), the DPP architecture incorporates a TTD network to generate frequency-dependent phase shifts, as illustrated in Fig. 4(b).

Compared with the energy-consuming method where all PSs are replaced with TTDs [43], the hybrid TTD-PS method in Fig. 4(b) makes a compromise between performance and hardware complexity by only employing a smaller number of TTDs to connect to all antennas to approach the optimal beamforming performance. To achieve this goal, the whole array is classified into multiple subarrays, each of which consists of several adjacent antenna elements. Since the antenna elements are closely distributed within each subarray, the difference between the required frequency-dependent and generated frequency-independent phase shifts is negligible. Thus, PSs are capable of approximating the required phase shifts. As a comparison, the difference between required frequency-dependent and generated frequency-independent phase shifts becomes significant between different subarrays, where TTDs become necessary to compensate for phase shift distortions. In such a manner, PSs and TTDs are combined to perform analog precoding. In this paper, we assume that each RF chain connects to K TTDs and each TTD connects to $P = \frac{N}{K}$ antennas in a sub-connected manner.

Based on the DPP architecture, the analog precoder could be expressed as the multiplication of the frequency-independent PS-based analog precoder and the frequency-dependent TTD-based analog precoder, written as

$$\begin{aligned}\mathbf{F}_{\mathrm{A}} &= \mathbf{F}_{\mathrm{A}}^{\mathrm{PS}}\mathbf{F}_{\mathrm{A},m}^{\mathrm{TTD}} \\ &= \left[\mathbf{F}_1^{\mathrm{PS}}, \cdots, \mathbf{F}_{N_{\mathrm{RF}}}^{\mathrm{PS}}\right] \begin{bmatrix} \mathbf{f}_{1,m}^{\mathrm{TTD}} & \cdots & \mathbf{0} \\ \vdots & \ddots & \vdots \\ \mathbf{0} & \cdots & \mathbf{f}_{N_{\mathrm{RF}},m}^{\mathrm{TTD}} \end{bmatrix},\end{aligned} \tag{9}$$

where $\mathbf{F}_{\mathrm{A}}^{\mathrm{PS}}$ and $\mathbf{F}_{\mathrm{A},m}^{\mathrm{TTD}}$ denote the analog precoding corresponding to the PS network and TTD network, respectively. In addition, $\mathbf{F}_l^{\mathrm{PS}} \in \mathbb{C}^{N\times K}$ and $\mathbf{f}_{l,m}^{\mathrm{TTD}} \in \mathbb{C}^{K\times 1}$ denote the l^{th} submatrix and l^{th} diagonal vector of $\mathbf{F}_{\mathrm{A}}^{\mathrm{PS}}$ and $\mathbf{F}_{\mathrm{A},m}^{\mathrm{TTD}}$, respectively. The subscript A is omitted in $\mathbf{F}_l^{\mathrm{PS}}$ and $\mathbf{f}_{l,m}^{\mathrm{TTD}}$ for illustration simplicity. Notations $\mathbf{F}_l^{\mathrm{PS}}$ and $\mathbf{f}_{l,m}^{\mathrm{TTD}}$ could be interpreted as the precoders of PSs and TTDs linking to the l^{th} RF chain in DPP architecture. Therefore, the total analog precoder corresponding to the l^{th} RF chain is written as $\mathbf{f}_l = \mathbf{F}_l^{\mathrm{PS}}\mathbf{f}_{l,m}^{\mathrm{TTD}}$, where $\mathbf{f}_l$ denotes the l^{th} column of $\mathbf{F}_{\mathrm{A}}$. Roughly speaking, the phase shifts generated by TTDs are linear to frequency[3].

[3]It is worth noting that a pure delay of TTD results in phase shifts in proportion to frequency [22]. Nevertheless, the frequency-independent term could be realized through PSs, which will be introduced in the next subsection. In this subsection, we relax the constraint of TTD units from in proportion to frequency to linear to frequency for illustration simplicity.

In addition, according to the connection relationship between TTDs and PSs, $\mathbf{F}_l^{\mathrm{PS}}$ is a block diagonal matrix as

$$\begin{aligned}\mathbf{F}_l^{\mathrm{PS}} &= \mathrm{blkdiag}\left[(\mathbf{f}_l^{\mathrm{PS}})_1, \cdots, (\mathbf{f}_l^{\mathrm{PS}})_K\right] \\ &= \begin{bmatrix} (\mathbf{f}_l^{\mathrm{PS}})_1 & \cdots & \mathbf{0} \\ \vdots & \ddots & \vdots \\ \mathbf{0} & \cdots & (\mathbf{f}_l^{\mathrm{PS}})_K \end{bmatrix},\end{aligned} \tag{10}$$

where $(\mathbf{f}_l^{\mathrm{PS}})_k \in \mathbb{C}^{P\times 1}$ denotes the analog precoder of PSs connecting to the k^{th} TTD.

Recall that the objective of the design of analog precoder $\mathbf{f}_l$ is to maximize the beamforming gain on l^{th} path of the channel, which is expressed by

$$\max_{\mathbf{f}_l} \; G_m(\mathbf{f}_l, \phi_l) = \max_{\mathbf{f}_l} \; \left|\mathbf{a}_m^H(\phi_l)\mathbf{f}_l\right|. \tag{11}$$

In such a way, different paths $l = 1, 2, \cdots, L$ could be compensated one by one with each RF chain.

It is worth noting that PSs could work well in narrowband systems but fail to meet the requirement of frequency-dependent phase shifts in wideband systems. A natural method is first designing PSs to align the beam towards the desired direction at the central frequency within each subarray, like in narrowband systems [22]. Then, the TTDs are designed to compensate for the frequency-dependent residual components between different subarrays, aiming to mitigate the beam defocus effect in wideband systems. Following this method, the analog precoder of PSs $\mathbf{F}_l^{\mathrm{PS}}$ could be initialized as

$$(\mathbf{f}_l^{\mathrm{PS}})_k = \mathbf{a}_c(\phi_l)_k, \tag{12}$$

where $\mathbf{a}_c(\phi_l)_k \in \mathbb{C}^{P\times 1}$ denotes the k^{th} subvector of $\mathbf{a}_c(\phi_l)$ in (3). Then, the analog precoder of TTDs could be obtained through the following lemma.

Lemma 3. The optimal $\mathbf{f}_{l,m}^{\mathrm{TTD}}$ compensating for the frequency-dependent residuals of the l^{th} path to maximize the beamforming gain could be expressed as

$$\left(\mathbf{f}_{l,m}^{\mathrm{TTD}}\right)_k = \exp\left\{j\frac{2\pi R}{c}(f_m - f_c)\cos\left(\phi_l - \bar{\theta}_k\right)\right\}, \tag{13}$$

where $\bar{\theta}_k = \frac{2\pi k}{K} + \frac{(P-1)\pi}{N}$, $(\mathbf{f}_{l,m}^{\mathrm{TTD}})_k$ denotes the k^{th} element of $\mathbf{f}_{l,m}^{\mathrm{TTD}}$. Thus, the beamforming gain at f_m is written as

$$G_m(\mathbf{f}_l, \phi_l) \approx \frac{1}{P}\sum_{p=0}^{P-1} J_0(R_p), \tag{14}$$

where $R_p = \frac{2\sqrt{2}\pi R}{c}(f_m - f_c)\sqrt{1 - \cos\left(\frac{(2p+1)\pi}{N} - \frac{\pi}{K}\right)}$ for $p = 0, 1, \cdots, P-1$.

Proof. The proof is provided in Appendix B. ■

The conclusion presented in **Lemma 3** aligns with the intuition that TTD should compensate for the frequency-dependent residuals at the *center* of each subarray to achieve maximum beamforming gain. It is noteworthy that, when $f_c = f_m$, no time delays are required. Furthermore, we would like to highlight that a large value of K is assumed in the proof of **Lemma 3** to obtain a relatively accurate approximation. Through this lemma, we can see that the beamforming gain after introducing the TTD network is highly dependent on the choice of K. Nevertheless, directly extracting the relationship between the beamforming gain and K proves challenging. Hence, we seek a more succinct expression of beamforming gain with the following corollary.

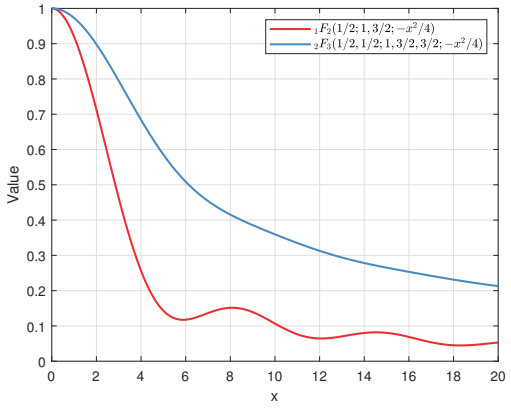

Fig. 5. Illustration of the generalized hypergeometric functions ${}_1F_2(\frac{1}{2};1,\frac{3}{2};-\frac{x^2}{4})$ and ${}_2F_3(\frac{1}{2},\frac{1}{2};1,\frac{3}{2},\frac{3}{2};-\frac{x^2}{4})$ against x.

Corollary 1. With the assumption of a large K, the beamforming gain with DPP architectures obtained in (14) could be further simplified into

$$G_m(\mathbf{f}_l, \phi_l) \approx \left|{}_1F_2\left(\frac{1}{2};1,\frac{3}{2};-\frac{a^2}{4}\right)\right|, \tag{15}$$

where the notation ${}_1F_2$ represents the generalized hypergeometric function [44] and $a = \frac{2\pi^2 R}{cK}(f_m - f_c)$.

Proof. The proof is provided in Appendix C. ■

Although the special function ${}_1F_2(\cdot)$ in (15) may appear complex, it is essentially a one-variable function over a, where an example of ${}_1F_2(\frac{1}{2};1,\frac{3}{2};-\frac{x^2}{4})$ against x is plotted as the red line in Fig. 5. Observing the overall decreasing trend of ${}_1F_2(\frac{1}{2};1,\frac{3}{2};-\frac{x^2}{4})$, we can tentatively conclude that a larger number of TTDs is required to further mitigate the beamforming loss. Then, a critical problem arises, how can we estimate the number of required TTDs to ensure that the beamforming loss remains below a predetermined threshold across the entire bandwidth? This problem will be discussed in the following corollary.

Corollary 2. Aiming to achieve a beamforming loss less than a threshold Δ in the entire bandwidth, the required number of TTDs has to satisfy

$$K \geq \frac{\pi^2 RB}{cF^{-1}(1-\Delta)}, \tag{16}$$

where the function $F^{-1}(1-\Delta)$ is defined by $F^{-1}(1-\Delta) \triangleq \arg\min_{x\geq 0}\left\{{}_1F_2(\frac{1}{2};1,\frac{3}{2};-\frac{x^2}{4}) = 1-\Delta\right\}$.

Proof. Note that $|f_c - f_m| \leq B/2$ always holds for any subcarrier f_m. By substituting the definitions of a and $F^{-1}(\cdot)$ into (15), the results in (16) can be easily obtained. ■

B. DPP Algorithm for UCA Systems

Based on the previous beamforming analysis with the DPP architecture, the complete precoding algorithm consisting of digital precoder and analog precoder implemented by both PSs and TTDs will be provided in this subsection.

Based on the TTD-PS architecture, the received signal can be rewritten as

$$\mathbf{y}_m = \sqrt{\rho}\mathbf{H}_m^H \mathbf{F}_{\mathrm{A}}^{\mathrm{PS}} \mathbf{F}_{\mathrm{A},m}^{\mathrm{TTD}} \mathbf{F}_{\mathrm{D},m} \mathbf{s}_m + \mathbf{n}_m. \tag{17}$$

According to the functional principle of TTD units, the phase shift generated by TTD has to be strictly proportional to frequency, written as $-2\pi f_m t$ where t denotes the time delay. Noticing that the optimal phase shifts in equation (13) have two separated components, written as

$$\begin{aligned} \angle\left(\mathbf{f}_{l,m}^{\mathrm{TTD}}\right)_k = &-\frac{2\pi R}{c}\cos\left(\phi_l - \bar{\theta}_k\right) f_c \\ &+ \frac{2\pi R}{c}\cos\left(\phi_l - \bar{\theta}_k\right) f_m, \end{aligned} \tag{18}$$

where the former is frequency-independent while the latter is exactly proportional to frequency f_m. Therefore, we can divide the required phase shifts into the frequency-independent component and frequency-dependent component, which can be realized by PSs and TTDs, respectively. Thus, the required time delay for the k^{th} TDD corresponding to the l^{th} channel component has to satisfy

$$-2\pi f_m t_{l,k} = \frac{2\pi R}{c}\cos\left(\phi_l - \bar{\theta}_k\right) f_m. \tag{19}$$

Then, we can obtain $t_{l,k} = -\frac{R}{c}\cos\left(\phi_l - \bar{\theta}_k\right)$. In addition, since the TTD has an additional constraint $t_l > 0$, a global time delay needs to be added to all TTDs without influencing the beamforming performance. The modified delay could be written as

$$t_{l,k} = \frac{R}{c}\left(1 - \cos\left(\phi_l - \bar{\theta}_k\right)\right). \tag{20}$$

Finally, the modified analog precoder corresponding to the TTD network is written as

$$\mathbf{f}_{l,m}^{\mathrm{TTD}} = [e^{-2\pi f_m t_{l,1}}, e^{-2\pi f_m t_{l,2}}, \cdots, e^{-2\pi f_m t_{l,K}}]^T. \tag{21}$$

So far, the frequency-dependent component of phase shifts has been addressed. After combining the frequency-independent component in (18) into the original analog precoder $\mathbf{F}_l^{\mathrm{PS}}$ in (12), the k^{th} diagonal vector of modified analog precoder corresponding to the PSs $\mathbf{F}_l^{\mathrm{PS}}$ can be finally written as

$$\left(\mathbf{f}_l^{\mathrm{PS}}\right)_k = \mathbf{a}_c(\phi_l)_k e^{-j\frac{2\pi R}{c}\cos(\phi_l - \bar{\theta}_k) f_c}. \tag{22}$$

The proposed DPP algorithm is summarized in **Algorithm 1**. Note that each RF chain is designed to cope with one channel path. We first rearrange the channel components in descending order, aiming to deal with the most significant channel components with limited RF chains, as shown in line 1. Then, according to the separation method of the required phase shift in (18), we can add phase shifts to the classical beam steering vector to obtain each column of the PS-based analog precoder, as shown in lines 3, 5, and 8. By extracting the frequency-dependent components, we can obtain the analog precoder associated with TTDs, as shown in lines 6 and 9. Then, by concatenating the derived precoders for each RF chain, the analog precoder can be obtained in lines 11-12. Finally, we can follow the water-filling procedure, using the equivalent channel and singular value decomposition (SVD) to obtain the digital precoders, as shown in lines 13-14 [45].

Remark 3. It is noteworthy that, the acquirement of all channel components, i.e. g_l and ϕ_l, is a precondition of the proposed DPP algorithm, which is often adopted as a basic condition in existing works [9], [22], [46]. Generally, the channel state information could be effectively obtained through compressive sensing methods [47] or deep learning methods [48] in wideband mmWave and THz communications.

In addition, the DPP algorithm is also feasible in the more practical uniform concentric circular array (UCCA) systems, where multiple UCAs with different radii are simultaneously employed to ensure a compact array geometry. In UCCA systems, different UCAs could be similarly partitioned into subarrays, where the corresponding analog precoders could be redesigned taking the different radii into consideration.

V. System Performance Analysis

In this section, the performance analysis on averaged beamforming gain and spectrum efficiency will be provided.

A. Averaged Beamforming Gain Performance

In Section IV-A, the beamforming gain at different frequencies with DPP architecture is investigated. Nevertheless, the analysis is only restricted to a single frequency, failing to reveal the overall beamforming performance across the entire bandwidth. To quantify how serious the beam defocus effect is in hybrid precoding architectures, we define the averaged beamforming gain under the single-path assumption as

$$\begin{aligned} G_{\mathrm{ave}}^{\mathrm{PS}} &= \frac{1}{B}\int_{f_c - B/2}^{f_c + B/2} \left|\mathbf{a}_m^H(\phi)\mathbf{a}_c(\phi)\right| \mathrm{d}f_m \\ &\overset{(a)}{\approx} \frac{1}{B}\int_{-B/2}^{B/2} \left| J_0\left(\frac{2\pi R}{c} f'_m\right)\right| \mathrm{d}f'_m, \end{aligned} \tag{23}$$

where approximation (a) is derived by substituting the results in (5) and defining $f'_m = f_m - f_c$. Due to the difficulty in directly addressing the integral of the absolute Bessel function, we instead analyze its upper and lower bound. According to the Cauchy-Schwarz inequality, the upper bound of (23) could be expressed as

$$\begin{aligned} G_{\mathrm{ave}}^{\mathrm{PS}} &\le \frac{1}{B}\sqrt{B\int_{-B/2}^{B/2} J_0^2\left(\frac{2\pi R}{c} f'_m\right) \mathrm{d}f'_m} \\ &= \sqrt{{}_2F_3\left(\frac{1}{2}, \frac{1}{2}; 1, \frac{3}{2}, \frac{3}{2}; -\frac{\pi^2 B^2 R^2}{4c^2}\right)}, \end{aligned} \tag{24}$$

where the proof is similar to Appendix C and thereby is omitted in this paper. Then, a simple lower bound could be obtained with the integration without the absolute operator, expressed as

$$\begin{aligned} G_{\mathrm{ave}}^{\mathrm{PS}} &\ge \frac{1}{B}\int_{-B/2}^{B/2} J_0\left(\frac{2\pi R}{c} f'_m\right) \mathrm{d}f'_m \\ &\overset{(b)}{\approx} {}_1F_2\left(\frac{1}{2}; 1, \frac{3}{2}; -\frac{\pi^2 B^2 R^2}{4c^2}\right), \end{aligned} \tag{25}$$

Algorithm 1 DPP algorithm for UCA.

Input: Channel $\mathbf{H}_m$, number of antennas N, RF chains N_{RF}, TTDs K, UCA radius R, frequency f_m and angles ϕ_l
Output: Analog precoder $\mathbf{F}_{\mathrm{A}}^{\mathrm{PS}}$ and $\mathbf{F}_{\mathrm{A},m}^{\mathrm{TTD}}$, digital precoder $\mathbf{F}_{\mathrm{D},m}$

Rearrange the order of the channel components $|g_1| \geq |g_2| \geq \cdots \geq |g_{\mathrm{RF}}|$ and obtain corresponding $\{\phi_1, \cdots, \phi_{\mathrm{RF}}\}$;
for $l = 1, 2, \cdots, N_{\mathrm{RF}}$ **do**
  Construct the beam steering vector $\mathbf{a}_c(\phi_l) = \frac{1}{\sqrt{N}} \left[e^{j\eta_c \cos(\phi_l - \psi_0)}, \cdots, e^{j\eta_c \cos(\phi_l - \psi_{N-1})}\right]^T$ as (3);
  for $k = 1, 2, \cdots, K$ **do**
    Append frequency-independent phase shifts $(\mathbf{f}_l^{\mathrm{PS}})_k = \mathbf{a}_c(\phi_l)_k e^{-j\frac{2\pi R}{c}\cos\left(\phi_l - \bar{\theta}_k\right) f_c}$ as (22);
    Determine the required delay for k^{th} TTD $t_{l,k} = \frac{R}{c}\left(1 - \cos\left(\phi_l - \bar{\theta}_k\right)\right)$ as (20);
  end for
  Construct the PS-based analog precoder for the l^{th} RF chain $\mathbf{F}_l^{\mathrm{PS}} = \mathrm{blkdiag}\left[(\mathbf{f}_l^{\mathrm{PS}})_1, \cdots, (\mathbf{f}_l^{\mathrm{PS}})_K\right]$ as (10);
  Construct the TTD-based analog precoder for the l^{th} RF chain $\mathbf{f}_{l,m}^{\mathrm{TTD}} = [e^{-2\pi f_m t_{l,1}}, \cdots, e^{-2\pi f_m t_{l,K}}]^T$ as (21);
end for
Concatenate PS-based analog precoders $\mathbf{F}_{\mathrm{A}}^{\mathrm{PS}} = \left[\mathbf{F}_1^{\mathrm{PS}}, \cdots, \mathbf{F}_{N_{\mathrm{RF}}}^{\mathrm{PS}}\right]$ as (9);
Concatenate TTD-based analog precoders $\mathbf{F}_{\mathrm{A},m}^{\mathrm{TTD}} = \mathrm{blkdiag}\left(\left[\mathbf{f}_{1,m}^{\mathrm{TTD}}, \cdots, \mathbf{f}_{N_{\mathrm{RF}},m}^{\mathrm{TTD}}\right]\right)$ as (9);
Obtain the equivalent channel $\mathbf{H}_{\mathrm{eq},m} = \mathbf{H}_m \mathbf{F}_{\mathrm{A}}^{\mathrm{PS}} \mathbf{F}_{\mathrm{A},m}^{\mathrm{TTD}}$ with $\mathbf{H}_{\mathrm{eq},m} = \mathbf{U}_{\mathrm{eq},m} \mathbf{\Sigma}_{\mathrm{eq},m} \mathbf{V}_{\mathrm{eq},m}^H$;
Determine the digital precoder $\mathbf{F}_{\mathrm{D},m} = \mathbf{V}_{\mathrm{eq},m} \mathbf{\Lambda}$;
return $\mathbf{F}_{\mathrm{A}}^{\mathrm{PS}}$, $\mathbf{F}_{\mathrm{A},m}^{\mathrm{TTD}}$ and $\mathbf{F}_{\mathrm{D},m}$.

where equation (b) could be obtained following equation (50).

With the DPP architecture, the averaged beamforming gain can be reformulated into

$$\begin{aligned} G_{\mathrm{ave}}^{\mathrm{TTD}} &= \frac{1}{B}\int_{-B/2}^{B/2} \left| {}_1F_2\left(\frac{1}{2}; 1, \frac{3}{2}; -\frac{\pi^4 R^2}{c^2 K^2 f_m'^2}\right)\right| \mathrm{d}f_m' \\ &= {}_2F_3\left(\frac{1}{2}, \frac{1}{2}; 1, \frac{3}{2}, \frac{3}{2}; -\frac{\pi^4 B^2 R^2}{4c^2 K^2}\right). \end{aligned} \tag{26}$$

An illustration of ${}_2F_3\left(\frac{1}{2}, \frac{1}{2}; 1, \frac{3}{2}, \frac{3}{2}; -\frac{x^2}{4}\right)$ can be found as the blue line in Fig. 5. It can be seen that due to the monotone decreasing property, a larger K will contribute to an improved beamforming gain. Therefore, with the same bandwidth, an efficient way to improve the beamforming performance is to increase the number of TTDs. A numerical comparison of the classical hybrid precoding and DPP architecture over averaged beamforming gain will be provided in Section VI.

B. Spectrum Efficiency Analysis

In addition to the analysis under the single-path assumption, in this subsection the spectrum efficiency analysis is provided under a more general multi-path scenario. The spectrum efficiency at the m^{th} subcarrier can be expressed as

$$R_m = \log_2\left(\left|\mathbf{I} + \frac{\rho}{N_s \sigma_n^2} \mathbf{H}_m^H \mathbf{F}_{\mathrm{A}} \mathbf{F}_{\mathrm{D},m} \mathbf{F}_{\mathrm{D},m}^H \mathbf{F}_{\mathrm{A}}^H \mathbf{H}_m\right|\right), \tag{27}$$

where $\mathbf{F}_{\mathrm{A}}$ can be further decomposed as $\mathbf{F}_{\mathrm{A}} = \mathbf{F}_{\mathrm{A}}^{\mathrm{PS}} \mathbf{F}_{\mathrm{A},m}^{\mathrm{TTD}}$. According to [5], when the number of RF chains exceeds the number of resolvable paths, the spatial multiplexing gain could be fully harvested. Then, by assuming SVD of the channel $\mathbf{H}_m^H = \mathbf{U}_m \mathbf{\Sigma}_m \mathbf{V}_m^H$ and extracting the most significant sub-channels as $\widetilde{\mathbf{\Sigma}}_m = [\mathbf{\Sigma}_m]_{1:N_{\mathrm{s}},1:N_{\mathrm{s}}}$ and $\widetilde{\mathbf{V}}_m = [\mathbf{V}_m]_{:,1:N_{\mathrm{s}}}$, the spectrum efficiency can be reformulated into

$$\begin{aligned} R_m &= \log_2\left(\left|\mathbf{I} + \frac{\rho}{N_s \sigma_n^2} \widetilde{\mathbf{\Sigma}}_m \widetilde{\mathbf{V}}_m^H \mathbf{F}_{\mathrm{A}} \mathbf{F}_{\mathrm{D},m} \mathbf{F}_{\mathrm{D},m}^H \mathbf{F}_{\mathrm{A}}^H \widetilde{\mathbf{V}}_m \widetilde{\mathbf{\Sigma}}_m^H\right|\right) \\ &= \log_2\left(\left|\mathbf{I} + \frac{\rho}{N_s \sigma_n^2} \widetilde{\mathbf{\Sigma}}_m^2 \mathbf{V}_{m,\mathrm{eq}}^H \mathbf{V}_{m,\mathrm{eq}}\right|\right), \end{aligned} \tag{28}$$

where $\mathbf{V}_{m,\mathrm{eq}} = \mathbf{F}_{\mathrm{D},m}^H \mathbf{F}_{\mathrm{A},m}^{\mathrm{TTD}H} \mathbf{F}_{\mathrm{A}}^{\mathrm{PS}H} \widetilde{\mathbf{V}}_m$. Adopting the linear transformation in [5] which reformulates the unitary matrix $\widetilde{\mathbf{V}}_m$ with an orthogonal list of steering vectors, expressed as

$$\widetilde{\mathbf{V}}_m \approx \mathbf{A}_{\mathrm{t},m} \mathbf{F}_{\mathrm{D,m}}^{\mathrm{opt}}, \tag{29}$$

where $\mathbf{A}_{\mathrm{t},m} = [\mathbf{a}_m(\phi_1), \cdots, \mathbf{a}_m(\phi_{N_{\mathrm{s}}})]$, $\mathbf{F}_{\mathrm{D,m}}^{\mathrm{opt}}$ denote the optimal digital precoder maximizing the spectrum efficiency [5]. When the number of antennas tends to infinity with fixed antenna spacing, i.e. the radius of UCA tends to infinity, the steering vectors could form an orthogonal basis[4], revealing that $\mathbf{A}_{\mathrm{t},m}$ is a unitary matrix. Since $\mathbf{A}_{\mathrm{t},m}$ and $\widetilde{\mathbf{V}}_m$ are both unitary, when $\mathbf{F}_{\mathrm{A}}^{\mathrm{PS}} \mathbf{F}_{\mathrm{A},m}^{\mathrm{TTD}} = \mathbf{A}_{\mathrm{t},m}$ and $\mathbf{F}_{\mathrm{D},m} = \mathbf{F}_{\mathrm{D,m}}^{\mathrm{opt}}$ are satisfied, the maximum spectrum efficiency could be obtained as

$$R_m^{\mathrm{opt}} = \log_2\left(\left|\mathbf{I} + \frac{\rho}{N_s \sigma_n^2} \widetilde{\mathbf{\Sigma}}_m^2\right|\right). \tag{30}$$

However, due to the beam defocus effect in UCA systems, $\mathbf{F}_{\mathrm{A}}^{\mathrm{PS}} \mathbf{F}_{\mathrm{A},m}^{\mathrm{TTD}} = \mathbf{A}_{\mathrm{t},m}$ could not be perfectly obtained. Therefore, the key factor influencing the spectrum efficiency lies in the analog beamforming gain, which can be expressed as

$$\begin{aligned} &\left(\mathbf{F}_{\mathrm{A},m}^{\mathrm{TTD}H} \mathbf{F}_{\mathrm{A}}^{\mathrm{PS}H} \mathbf{A}_{\mathrm{t},m}\right)^H \mathbf{F}_{\mathrm{A},m}^{\mathrm{TTD}H} \mathbf{F}_{\mathrm{A}}^{\mathrm{PS}H} \mathbf{A}_{\mathrm{t},m} \\ &= \mathrm{blkdiag}\left(\left[G_m^2(\mathbf{f}_1, \phi_1), \cdots, G_m^2(\mathbf{f}_{N_{\mathrm{s}}}, \phi_{N_{\mathrm{s}}})\right]\right). \end{aligned} \tag{31}$$

In addition, note that the beamforming gain $G_m(\mathbf{f}_l, \phi_l)$ is independent of the angle. Therefore, the spectrum efficiency with the DPP architecture can be estimated by

$$\begin{aligned} R_m &\overset{(a)}{=} \log_2\left(\left|\mathbf{I} + \frac{\rho}{N_s \sigma_n^2} G_m^2(\mathbf{f}_l, \phi_l) \mathbf{\Sigma}_m^2\right|\right) \\ &\overset{(b)}{=} \log_2\left(\left|\mathbf{I} + \frac{\rho}{N_s \sigma_n^2} {}_1F_2\left(\frac{1}{2}; 1, \frac{3}{2}; -\frac{a^2}{4}\right)^2 \mathbf{\Sigma}_m^2\right|\right), \end{aligned} \tag{32}$$

where equation (a) is obtained according to the independence of G_m and ϕ_l and approximation (b) is derived from the

[4]Although this conclusion was originally derived in ULA systems, the asymptotic orthogonality of beam steering vectors could also be proved in UCA systems, see [42].

TABLE I
SIMULATION PARAMETERS

Central frequency f_c	30 GHz
Bandwidth B	0.1 $\sim$ 5 GHz
Number of subcarriers M	128
Number of paths L	4
Number of antennas at BS N	256
Number of antennas at user N_{r}	4
Number of data streams N_{s}	4
Number of TTDs K	1 $\sim$ 32

conclusion in **Corollary 1**. The variable $a = \frac{2\pi^2 R}{cK}(f_m - f_c)$ is only determined by the system settings. With a larger K, the spectrum efficiency is expected to be enhanced compared with the classical hybrid precoding architecture[5].

VI. SIMULATION RESULTS

In this section, simulation results are provided to validate the effectiveness of our theoretical analysis in previous sections. We consider a mmWave wideband communication system, where the simulation parameters are summarized in Table I.

The baselines include the optimal fully-digital precoding, the wideband optimization-based method [15], and steering vector-based methods aiming to alleviate the beam split effect [16]. In specific, the averaged covariance of the channel is calculated over the whole bandwidth, and the analog precoder is selected as the eigenvectors of the covariance matrix in [15]. The steering vector-based methods consist of selecting the single beam steering vector and combining multiple steering vectors to design the analog precoder. For the former, the steering vector at the central frequency is employed as the analog precoder, aiming to ensure optimal beamforming gain at the central frequency. While for the latter, the analog precoder is determined with the summation of multiple beam steering vectors, aiming to generate a wide beam with a balanced performance at chosen subcarriers.

According to the analysis in **Corollary 2**, if we aim to ensure a beamforming loss less than $\Delta = 40\%$, the minimum required number of TTDs could be calculated with (16) as 8.2. Since the number of TTDs has to be an integer, 8 TTDs are employed in this simulation. The beamforming gain with and without DPP is plotted in Fig. 6. It is shown that the introduction of DPP has significantly improved the beamforming performance compared with the PS-based hybrid precoding architectures, representing the classical hybrid precoding scheme without TTDs and employing the beam steering vector at the central frequency for beamforming. The beamforming gain has approximately exceeded the predetermined threshold of 0.6 over the bandwidth, indicating the effectiveness of the results in **Corollary 2**. In addition, the green dashed line perfectly

[5]It is noteworthy that the introduction of TTDs may result in additional insertion loss in the link budget, which requires compensation amplification with power amplifiers. In addition, the employed adjustable TTDs may introduce significant power consumption, reducing the system's energy efficiency. Other energy-efficient alternates of adjustable TTDs, such as fixed TTDs in [9], could be incorporated to improve the energy efficiency in UCA communications.

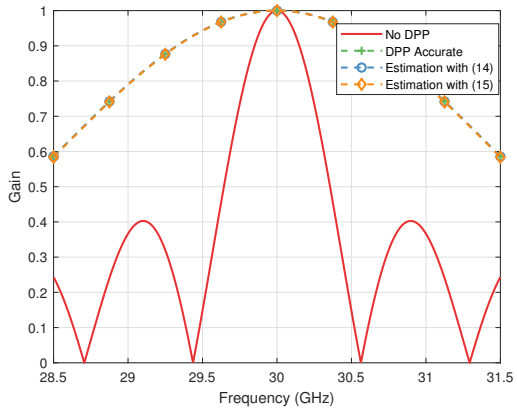

Fig. 6. Illustration of the beamforming gain with DPP architectures.

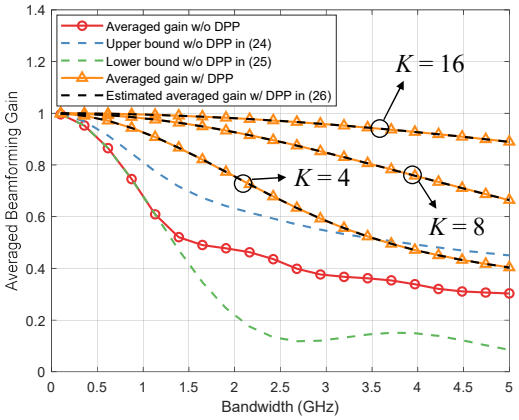

Fig. 7. Comparison on the averaged beamforming gain.

covers blue and black lines, revealing that approximations in (14) and (15) have achieved a high level of accuracy.

To show the superiority of DPP in improving the averaged beamforming gain, the comparisons between different architectures are plotted in Fig. 7, where the bandwidth B varies from 0.1 GHz to 5 GHz. It shows that the DPP architecture obtains the same performance as classical hybrid precoding architectures with a narrow bandwidth. As the bandwidth scales up, the employed DPP architecture always outperforms the classical hybrid precoding scheme. For a bandwidth $B = 2$ GHz, the DPP architecture with $K = 16$ TTDs could improve the averaged beamforming gain compared with the one without DPP by about 105%. The upper and lower bound of the averaged beamforming gain are also verified effective.

Then, the comparison of the spectrum efficiency over different SNRs is plotted in Fig. 8, where the number of TTDs and bandwidth are set to $K = 16$ and $B = 3$ GHz, respectively. It can be seen that the analysis of (32) achieves good accuracy. The small gap between the estimated and actual performance stems from that $\mathbf{A}_{\mathrm{t},m}$ in (29) is not a perfect unitary matrix, since the number of antennas is actually not infinite. Thus, estimation in (32) represented by the green line produces a slightly higher spectrum efficiency compared with the actual performance represented by the red line. In addition, the DPP method outperforms the optimization-based method and steering vector-based methods at different SNRs. The reason lies in that the analog precoder in the optimization-based

This article has been accepted for publication in IEEE Transactions on Communications. This is the author's version which has not been fully edited and content may change prior to final publication. Citation information: DOI 10.1109/TCOMM.2024.3354199

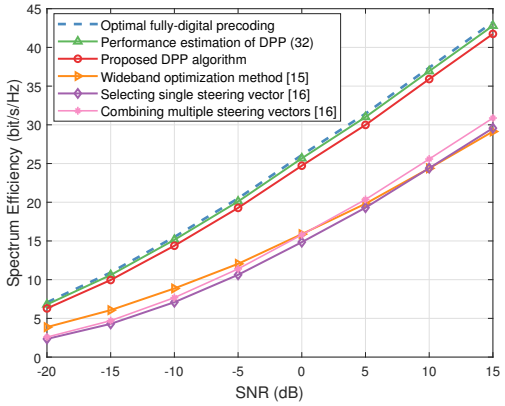

Fig. 8. Comparison on the spectrum efficiency over different SNRs.

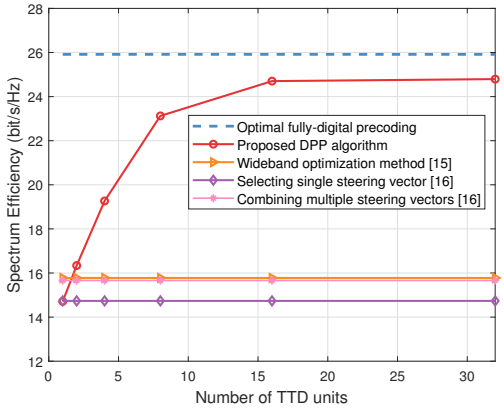

Fig. 9. Comparison on the spectrum efficiency over different number of TTDs.

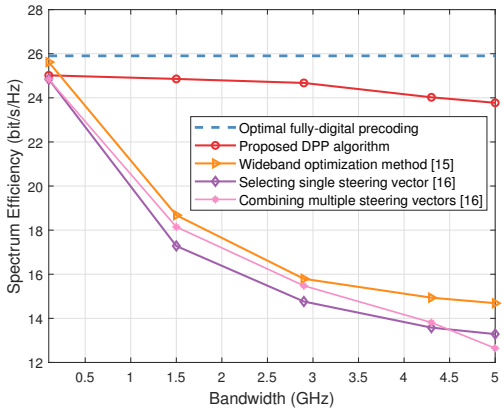

Fig. 10. Comparison on the spectrum efficiency over different bandwidths.

method is only designed to achieve a balanced but not ideal beamforming gain over the whole bandwidth, which could not obtain a maximized beamforming gain at each frequency. The methods of selecting single and multiple steering vectors still employ the frequency-independent phase shifters, which could not eliminate the beam defocus effect. In contrast, the DPP architecture is capable of generating frequency-dependent phase shifts with the aid of TTD, which is anticipated to be closer to the optimal beamforming gain at each frequency.

To demonstrate the impact of the number of TTDs, the system performance against K ranging from 1 to 32 with bandwidth $B = 3$ GHz is plotted in Fig. 9. It can be seen that, if only one TTD is employed, the performance of the DPP architecture is comparable to selecting single steering vector in hybrid precoding architectures. The performance of DPP improves as the number of TTDs scales up. When the number of TTDs satisfies $K \geq 8$, the spectrum efficiency of DPP has obtained over 90% of the optimal spectrum efficiency.

To show the influence of the bandwidth, the spectrum efficiency versus the bandwidth from 0.1 GHz to 5 GHz is plotted in Fig. 10. In this simulation, the number of TTDs is set to $K = 16$. With a narrow bandwidth, the optimization-based method could achieve near-optimal performance. Nevertheless, the performance of the optimization-based method will degrade as the bandwidth increases, indicating the influence of the spatial wideband effect in classical hybrid precoding architectures. On the contrary, the DPP method could obtain a relatively stable performance for different bandwidths. The performance of DPP architecture begins to decrease only when bandwidth exceeds 2.5 GHz, which indicates that DPP architecture is feasible to cope with a relatively large bandwidth.

VII. Conclusion

In this paper, the mechanism of the beam defocus effect in UCA systems is investigated for the first time. The dispersed beam pattern in the angular and frequency domain is characterized, revealing that the hybrid precoding architecture may face significant beamforming loss in UCA wideband communications. To retrieve an ideal beamforming gain, the DPP architecture and corresponding precoding algorithm are introduced to mitigate the beam defocus effect in UCA systems. Theoretical analysis and simulation results are provided to verify the effectiveness of the proposed method. The influence of the finite resolution of TTDs in UCA wideband communications is left for future research. Despite the feasibility of the proposed method in practical UCCA systems, a rigorous evaluation of the proposed method and the hardware implementation in UCCA are also worth investigating in the future. In addition, the energy efficiency analysis and the investigation to improve this indicator are also left for future research.

Appendix A
Proof of Lemma 2

The proof of **Lemma 2** also utilizes the generating function of Bessel functions. First, equation (7) could be written as

$$\begin{aligned} G_m(\mathbf{a}_c(\phi_0),\phi) &= \left|\mathbf{a}_m^H(\phi)\mathbf{a}_c(\phi_0)\right| \\ &= \left|\frac{1}{N}\sum_{n=0}^{N-1} e^{j[\eta_m\cos(\phi-\psi_n)-\eta_c\cos(\phi_0-\psi_n)]}\right|. \end{aligned} \tag{33}$$

With the Jacobi-Anger expansion of Bessel functions written as [41]

$$e^{j\beta\cos\gamma} = \sum_{s=-\infty}^{\infty} j^s J_s(\beta) e^{js\gamma}, \tag{34}$$

equation (33) could be rewritten as

$$\begin{aligned} G_m(\mathbf{a}_c(\phi_0),\phi) &= \frac{1}{N}\left|\sum_{n=0}^{N-1}\left[\sum_{s_1=-\infty}^{+\infty} j^{s_1}J_{s_1}(\eta_m)e^{js_1(\phi-\psi_n)}\right]\right. \\ &\quad \left.\times\left[\sum_{s_2=-\infty}^{+\infty} j^{s_2}J_{s_2}(-\eta_c)e^{js_2(\phi_0-\psi_n)}\right]\right| \\ &\overset{(a)}{=} \frac{1}{N}\left|\sum_{s_1=-\infty}^{+\infty}\sum_{s_2=-\infty}^{+\infty} j^{s_1+s_2}J_{s_1}(\eta_m)J_{s_2}(-\eta_c)\right. \\ &\quad \left.\times e^{j(s_1\phi+s_2\phi_0)}\sum_{n=0}^{N-1} e^{-j(s_1+s_2)\psi_n}\right|, \end{aligned} \tag{35}$$

where equation (a) is obtained by exchanging the order of the three summations. When replacing ψ_n with $\frac{2\pi n}{N}$, the last summation over n could be expressed as the piecewise function as

$$\sum_{n=0}^{N-1} e^{-j(s_1+s_2)\psi_n} = \begin{cases} N, & s_1+s_2 = N\cdot t, t\in\mathbb{Z} \\ 0, & s_1+s_2 \neq N\cdot t, t\in\mathbb{Z}. \end{cases} \tag{36}$$

Similar to the proof process of **Lemma 1**, the conditions of $s_1+s_2\neq 0$ could be omitted in the summation when assuming a large N. Substituting $s_1+s_2=0$, the beamforming gain could be simplified into

$$\begin{aligned} G_m(\mathbf{a}_c(\phi_0),\phi) &= \left|\sum_{s=-\infty}^{+\infty} J_s(\eta_m)J_{-s}(-\eta_c)e^{js(\phi-\phi_0)}\right| \\ &\overset{(b)}{=} \left|\sum_{s=-\infty}^{+\infty} J_s(\eta_m)J_s(\eta_c)e^{js(\phi-\phi_0)}\right|, \end{aligned} \tag{37}$$

where equation (b) is derived with the property $J_s(-x) = (-1)^s J_s(x)$ and $J_{-s}(x) = (-1)^s J_s(x)$ [49]. In addition, according to the Addition Theorems of Bessel functions [49]

$$J_0(r_0) = \sum_{s=-\infty}^{+\infty} J_s(r_1)J_s(r_2)e^{js\theta}, \tag{38}$$

where $r_0 = \sqrt{r_1^2+r_2^2-2r_1r_2\cos\theta}$, the beamforming gain could be rewritten in a concise expression as

$$G_m(\mathbf{a}_c(\phi_0),\phi) = |J_0(\xi)|, \tag{39}$$

where $\xi = \sqrt{\eta_m^2+\eta_c^2-2\eta_m\eta_c\cos(\phi-\phi_0)}$. This completes the proof.

Appendix B
Proof of Lemma 3

With $\mathbf{a}_c^{(t)}(\phi)$, the n^{th} element of product of beamforming vector and steering vector at m^{th} subcarrier is written as

$$\left[\mathbf{a}_m^H(\phi)\mathbf{a}_c(\phi)\right]_n = e^{j\frac{2\pi R}{c}(f_c-f_m)\cos(\phi-\frac{2\pi n}{N})}, \tag{40}$$

where $n = 0,1,\cdots,N-1$. Noticing that the frequency-dependent phase shifts are not needed at central frequency, $\mathbf{f}_{l,m}^{\text{TTD}}$ should be equal to $\mathbf{0}$ when $f_m = f_c$. In addition, when each antenna is equipped with an individual TTD unit, no beam defocus will be generated. Therefore, the corresponding value of $\mathbf{f}_{l,m}^{\text{TTD}}$ should be written as

$$\mathbf{f}_{l,m}^{\text{TTD}} = \left[e^{j\frac{2\pi R(f_m-f_c)}{c}\cos\phi},\cdots,e^{j\frac{2\pi R(f_m-f_c)}{c}\cos(\phi-\frac{2\pi(N-1)}{N})}\right]. \tag{41}$$

Following this intuition, the k^{th} element of $\mathbf{f}_{l,m}^{\text{TTD}}$ for connecting to K TTDs should also be expressed as $e^{j\frac{2\pi R}{c}(f_m-f_c)\cos(\phi-\bar{\theta}_k)}$, where $\bar{\theta}_k$ denotes the specific phase shift corresponding to the k^{th} subarray.

Then, the beamforming gain with DPP architectures could be reformulated as

$$\begin{aligned} G_m(\mathbf{f}_l,\phi) = \frac{1}{N}\sum_{k=0}^{K-1}\left[\sum_{i=kP}^{(k+1)P-1} e^{j\frac{2\pi R}{c}(f_c-f_m)\cos(\phi-\frac{2\pi i}{N})}\right. \\ \left.\times e^{j\frac{2\pi R}{c}(f_m-f_c)\cos(\phi-\bar{\theta}_k)}\right]. \end{aligned} \tag{42}$$

Then, again with the Jacobi-Anger expansion in (34), we can rewrite the inner summation over i as

$$\begin{aligned} &\sum_{i=kP}^{(k+1)P-1} e^{j\frac{2\pi R}{c}(f_c-f_m)\cos(\phi-\frac{2\pi i}{N})} \\ &\overset{(a)}{=} \sum_{s_1=-\infty}^{+\infty} j^{s_1}J_{s_1}\left(\frac{2\pi R}{c}(f_c-f_m)\right)e^{js_1\phi}\sum_{i=kP}^{(k+1)P-1} e^{-js_1\frac{2\pi i}{N}}, \end{aligned} \tag{43}$$

where the equation (a) is obtained by substituting the generating function. Similarly, the outer summation over k could be written as

$$\begin{aligned} &\sum_{k=0}^{K-1} e^{j\frac{2\pi R}{c}(f_m-f_c)\cos(\phi-\bar{\theta}_k)}\sum_{i=kP}^{(k+1)P-1} e^{-js_1\frac{2\pi i}{N}} \\ &= \sum_{s_2=-\infty}^{+\infty} j^{s_2}J_{s_2}\left(\frac{2\pi R}{c}(f_m-f_c)\right)e^{js_2\phi} \\ &\quad\times\sum_{k=0}^{K-1} e^{-js_2\bar{\theta}_k}\sum_{i=kP}^{(k+1)P-1} e^{-js_1\frac{2\pi i}{N}} \\ &\overset{(b)}{=} \sum_{s_2=-\infty}^{+\infty} j^{s_2}J_{s_2}\left(\frac{2\pi R}{c}(f_m-f_c)\right)e^{js_2\phi} \\ &\quad\times\frac{1-e^{-js_1 2\pi/K}}{1-e^{-js_1 2\pi/N}}e^{-js_2\frac{\xi}{K}}\sum_{k=0}^{K-1} e^{-j(s_1+s_2)\frac{2\pi k}{K}}, \end{aligned} \tag{44}$$

where the equation (b) is derived by assuming $\bar{\theta}_k = \frac{2\pi k}{K}+\frac{\xi}{K}$. Then we can adopt a similar process as the proof of **Lemma 1.** by setting $s_1+s_2=0$ assuming a relatively large K. The beamforming gain could be finally simplified as

$$\begin{aligned} &G_m(\mathbf{f}_l,\phi) \\ &= \frac{1}{P}\sum_{s=-\infty}^{+\infty} J_s^2\left(\frac{2\pi R}{c}(f_c-f_m)\right)\sum_{p=0}^{P-1} e^{-js\frac{2\pi p-P\xi}{N}} \\ &= \frac{1}{P}\sum_{p=0}^{P-1}\sum_{s=-\infty}^{+\infty} J_s^2\left(\frac{2\pi R}{c}(f_c-f_m)\right)e^{-js\frac{2\pi p-P\xi}{N}} \\ &\overset{(c)}{=} \frac{1}{P}\sum_{p=0}^{P-1} J_0(R_p), \end{aligned} \tag{45}$$

where equation (c) is derived with the Addition Theorems [49] and $R_p = \frac{2\sqrt{2}\pi R}{c}(f_c-f_m)\sqrt{1-\cos\left(\frac{2\pi p}{N}-\frac{\xi}{K}\right)}$. Finally, the beamforming gain could be approximately maximized when $\xi = \pi-\frac{\pi}{P}$, which makes R_p as small as possible.

APPENDIX C
PROOF OF COROLLARY 1

We first denote $\zeta_i = \frac{(2i+1)\pi}{N} - \frac{\pi}{K}$ for $i = 0, 1, \cdots, P-1$. As a result, ζ_i satisfies $\zeta_i \in \left[-\frac{\pi}{K} + \frac{\pi}{N}, \frac{\pi}{K} - \frac{\pi}{N}\right]$. Assuming a large K, ζ_i can be viewed to around 0. With the Taylor series expansion $\cos(x) = 1 - \frac{1}{2}x^2 + \mathcal{O}(x^2)$, R_i in (14) could be simplified as

$$R_i = \frac{2\sqrt{2}\pi R}{c}(f_c - f_m)\sqrt{1-\cos\zeta_i} \overset{(a)}{\approx} \frac{2\pi R}{c}(f_c - f_m)\zeta_i, \tag{46}$$

where $i = 0, 1, \cdots, P-1$. Then, the beamforming gain could be rewritten as

$$\begin{aligned} G_m(\mathbf{f}_l, \phi) &= \frac{1}{P}\sum_{i=0}^{P-1} J_0\left(\frac{2\pi R}{c}(f_c - f_m)\zeta_i\right) \\ &\overset{(b)}{\approx} \frac{N}{2\pi P}\int_{-\pi/K}^{\pi/K} J_0\left(\frac{2\pi R}{c}(f_c - f_m)\zeta\right)\mathrm{d}\zeta \\ &\overset{(c)}{=} \frac{N}{\pi P}\int_{0}^{\pi/K} J_0\left(\frac{2\pi R}{c}(f_c - f_m)\zeta\right)\mathrm{d}\zeta, \end{aligned} \tag{47}$$

where approximation (b) is obtained by replacing summation with integral over ζ. Equation (c) is derived according to the parity of $J_0(\cdot)$. By substituting $\zeta' = \frac{2\pi R}{c}(f_c - f_m)\zeta$ and $a = \frac{\pi}{K}\cdot\frac{2\pi R}{c}(f_c - f_m)$, the above equation could be further simplified into

$$G_m(\mathbf{f}_l, \phi) \approx \frac{1}{a}\int_0^a J_0(\zeta')\,\mathrm{d}\zeta' \overset{(d)}{=} {}_1F_2\left(\frac{1}{2}; 1, \frac{3}{2}; -\frac{a^2}{4}\right), \tag{48}$$

where the proof of equation (d) shall be shown as follows. According to the definition, $\int_0^a J_0(x)\mathrm{d}x$ could be expressed as

$$\begin{aligned} \frac{1}{a}\int_0^a J_0(x)\mathrm{d}x &= \frac{1}{a}\sum_{n=0}^{\infty}(-1)^n\frac{1}{2^{2n}\Gamma^2(n+1)}\int_0^a x^{2n}\mathrm{d}x \\ &= \sum_{n=0}^{\infty}(-1)^n\frac{1}{(2n+1)2^{2n}\Gamma^2(n+1)}a^{2n}. \end{aligned} \tag{49}$$

While according to the definition of generalized hypergeometric function and the notation $(a)_n = a(a+1)\cdots(a+n-1)$ for $n \geq 1$, function ${}_1F_2\left(\frac{1}{2}; 1, \frac{3}{2}; -\frac{a^2}{4}\right)$ could be expressed

$$\begin{aligned} {}_1F_2\left(\frac{1}{2}; 1, \frac{3}{2}; -\frac{a^2}{4}\right) &= \sum_{n=0}^{\infty}\frac{(\frac{1}{2})_n}{(1)_n(\frac{3}{2})_n}\cdot(-1)^n\frac{a^{2n}}{2^{2n}n!} \\ &= \sum_{n=0}^{\infty}(-1)^n\frac{a^{2n}}{2^{2n}(2n+1)n!n!} \\ &= \frac{1}{a}\int_0^a J_0(x)\mathrm{d}x, \end{aligned} \tag{50}$$

which completes the proof.

REFERENCES

[1] I. Ahmed, H. Khammari, A. Shahid, A. Musa, K. S. Kim, E. D. Poorter, , and I. Moerman, "A survey on hybrid beamforming techniques in 5G: Architecture and system model perspectives," *IEEE Commun. Surveys Tuts.*, vol. 20, no. 4, pp. 3060–3097, 4th Quart. 2018.

[2] S. Han, C.-L. I, Z. Xu, and C. Rowell, "Large-scale antenna systems with hybrid analog and digital beamforming for millimeter wave 5G," *IEEE Commun. Mag.*, vol. 53, no. 1, pp. 186–194, Jan. 2015.

[3] Y. Zhao, W. Xu, J. Xu, S. Jin, K. Wang, and M.-S. Alouini, "Analog versus hybrid precoding for multiuser massive MIMO with quantized CSI feedback," *IEEE Commun. Lett.*, vol. 24, no. 10, pp. 2319–2323, 2020.

[4] L. Yan, C. Han, and J. Yuan, "A dynamic array-of-subarrays architecture and hybrid precoding algorithms for terahertz wireless communications," *IEEE J. Sel. Areas Commun.*, vol. 38, no. 9, pp. 2041–2056, Sep. 2020.

[5] O. Ayach, S. Rajagopal, S. Abu-Surra, Z. Pi, and R. W. Heath, "Spatially sparse precoding in millimeter wave MIMO systems," *IEEE Trans. Wireless Commun.*, vol. 13, no. 3, pp. 1499–1513, Jan. 2014.

[6] X. Yu, J. Z. J. Shen, and K. B. Letaief, "Alternating minimization algorithms for hybrid precoding in millimeter wave MIMO systems," *IEEE J. Sel. Areas Commun.*, vol. 10, no. 3, pp. 485–500, Apr. 2016.

[7] X. Gao, L. Dai, S. Han, C.-L. I, and R. W. Heath, "Energy-efficient hybrid analog and digital precoding for mmwave MIMO systems with large antenna arrays," *IEEE J. Sel. Areas Commun.*, vol. 34, no. 4, pp. 998–1009, Apr. 2016.

[8] A. F. Molisch, V. V. Ratnam, S. Han, Z. Li, S. L. H. Nguyen, L. Li, , and K. Haneda, "Hybrid beamforming for massive MIMO: A survey," *IEEE Commun. Mag.*, vol. 55, no. 9, pp. 134–141, Sep. 2017.

[9] L. Yan, C. Han, and J. Yuan, "Energy-efficient dynamic-subarray with fixed true-time-delay design for terahertz wideband hybrid beamforming," *IEEE J. Sel. Areas Commun.*, vol. 40, no. 10, pp. 2840–2854, Oct. 2022.

[10] I.-S. Kim and J. Choi, "Spatial wideband channel estimation for mmWave massive MIMO systems with hybrid architectures and low-resolution ADCs," *IEEE Trans. Wireless Commun.*, vol. 20, no. 6, pp. 4016–4029, Jun. 2021.

[11] M. Jian, N. Zhang, and Y. Chen, "RIS: Spatial-wideband effect analysis and off-grid channel estimation," *ZTE Communications*, vol. 20, no. 1, pp. 57–62, 2022.

[12] Q. Wan, J. Fang, Z. Chen, and H. Li, "Hybrid precoding and combining for millimeter wave/sub-THz MIMO-OFDM systems with beam squint effects," *IEEE Trans. Veh. Technol.*, vol. 70, no. 8, pp. 8314–8319, Aug. 2021.

[13] Z. Li, Z. Gao, and T. Li, "Sensing user's channel and location with terahertz extra-large reconfigurable intelligent surface under hybrid-field beam squint effect," *IEEE J. Sel. Topics Signal Process.*, pp. 1–16, 2023.

[14] A. Alkhateeb and R. W. Heath, "Frequency selective hybrid precoding for limited feedback millimeter wave systems," *IEEE Trans. Commun.*, vol. 64, no. 5, pp. 1801–1818, May 2016.

[15] S. Park, A. Alkhateeb, and R. W. Heath, "Dynamic subarrays for hybrid precoding in wideband mmwave MIMO systems," *IEEE Trans. Wireless Commun.*, vol. 16, no. 5, pp. 2907–2920, May 2017.

[16] Y. Chen, Y. Xiong, D. Chen, T. Jiang, S. X. Ng, and L. Hanzo, "Hybrid precoding for wideband millimeter wave MIMO systems in the face of beam squint," *IEEE Trans. Wireless Commun.*, vol. 20, no. 3, pp. 1847–1860, Mar. 2021.

[17] Y. Chen, D. Chen, T. Jiang, and L. Hanzo, "Channel-covariance and angle-of-departure aided hybrid precoding for wideband multiuser millimeter wave MIMO systems," *IEEE Trans. Commun.*, vol. 67, no. 12, pp. 8315–8328, Dec. 2019.

[18] X. Liu and D. Qiao, "Space-time block coding-based beamforming for beam squint compensation," *IEEE Wireless Commun. Lett.*, vol. 8, no. 1, pp. 241–244, Feb. 2019.

[19] D. Hunter, M. Parker, and J. Dexter, "Demonstration of a continuously variable true-time delay beamformer using a multichannel chirped fiber grating," *IEEE Trans. Microw. Theory Tech.*, vol. 54, no. 2, pp. 861–867, Feb. 2006.

[20] M. Longbrake, "True time-delay beamsteering for radar," in *Proc. IEEE NAECON.*, Feb. 2012, pp. 246–249.

[21] R. J. Mailloux, *Phased Array Antenna Handbook, Second Edition*. Artech house, 2005.

[22] L. Dai, J. Tan, Z. Chen, and H. V. Poor, "Delay-phase precoding for wideband thz massive MIMO," *IEEE Trans. Wireless Commun.*, vol. 21, no. 9, pp. 7271–7286, Sep. 2022.

[23] M. Agiwal, A. Roy, and N. Saxena, "Next generation 5G wireless networks: A comprehensive survey," *IEEE Commun. Surveys Tuts.*, vol. 18, no. 3, pp. 1617–1655, Feb. 2016.

[24] J. Zhang, X. Ge, Q. Li, M. Guizani, and Y. Zhang, "5G millimeter-wave antenna array: Design and challenges," *IEEE Wireless Commun.*, vol. 24, no. 2, pp. 106–112, Apr 2017.

[25] S. M. Razavizadeh, M. Ahn, and I. Lee, "Three-dimensional beamforming: A new enabling technology for 5G wireless networks," *IEEE Signal Process. Mag.*, vol. 31, no. 6, pp. 94–101, Oct. 2014.

[26] W. Tan and S. Ma, "Antenna array topologies for mmWave massive MIMO systems: Spectral efficiency analysis," *IEEE Trans. Veh. Technol.*, vol. 71, no. 12, pp. 12 901–12 915, Dec. 2022.
[27] X. Cheng, Y. He, and J. Qiao, "Channel modeling for UCA and URA massive MIMO systems," in *Proc. Int. Conf. Comput., Netw. and Commun. (ICNC)*, 2020, pp. 963–968.
[28] A. Riadi, M. Boulouird, and M. M. R. Hassani, "Massive-MIMO configuration of multipolarized ULA and UCA in 5G wireless communications," in *Proc. 3rd Int. Conf. Netw. Inf. Syst. Secur.*, 2020, pp. 1–5.
[29] V. Kallnichev, "Analysis of beam-steering and directive characteristics of adaptive antenna arrays for mobile communications," *IEEE Antennas Propag. Mag.*, vol. 43, no. 3, pp. 145–152, Jun. 2001.
[30] J. H. Kim, W. Jeon, and S.-Y. Chung, "Asymptotic analysis on directivity and beamwidth of uniform circular array," *IEEE Antennas Wireless Propag. Lett.*, vol. 16, pp. 3092–3095, Oct. 2017.
[31] A. Koc, A. Masmoudi, and T. Le-Ngoc, "Hybrid beamforming for uniform circular arrays in multi-user massive MIMO systems," in *Proc. IEEE Can. Conf. of Electr. and Comput. Eng. (CCECE)*, 2019, pp. 1–4.
[32] M. Mahmood, A. Koc, and T. Le-Ngoc, "Energy-efficient MU-massive-MIMO hybrid precoder design: Low-resolution phase shifters and digital-to-analog converters for 2D antenna array structures," *IEEE Open J. Commun. Soc.*, vol. 2, pp. 1842–1861, Aug. 2021.
[33] Y. Zhang, R. Woods, Y. Ko, A. Marshall, and J. Zhang, "Security optimization of exposure region-based beamforming with a uniform circular array," *IEEE Trans. Commun.*, vol. 66, no. 6, pp. 2630–2641, Jun. 2018.
[34] Y. He, C.-X. Wang, H. Chang, R. Feng, J. Sun, W. Zhang, Y. Hao, and E.-H. M. Aggoune, "A novel 3-D beam domain channel model for maritime massive MIMO communication systems using uniform circular arrays," *IEEE Trans. Commun.*, vol. 71, no. 4, pp. 2487–2502, Apr. 2023.
[35] S. C. Chan and H. H. Chen, "Uniform concentric circular arrays with frequency-invariant characteristics—theory, design, adaptive beamforming and doa estimation," *IEEE Trans. Signal Process.*, vol. 55, no. 1, pp. 165–177, Jan. 2007.
[36] I. Carton, W. Fan, and G. F. Pedersen, "A frequency invariant beamformer for channel parameter estimation in millimeter wave bands," in *Proc. IEEE Int. Symp. Antennas Propag. (ISAP)*, 2015, pp. 1–4.
[37] Z. Yuan, F. Zhang, Y. Zhang, J. Zhang, G. F. Pedersen, and W. Fan, "On phase mode selection in frequency invariant beamformer for near-field mmwave channel characterization," *IEEE Trans. Antennas Propag.*, pp. 1–1, Sep. 2023.
[38] J. Wang, F. Yang, and J. Yang, "Insights into the MMSE-based frequency-invariant beamformers for uniform circular arrays," *IEEE Signal Process. Lett.*, vol. 29, pp. 2432–2436, Nov. 2022.
[39] F. Zhang and W. Fan, "Near-field ultra-wideband mmwave channel characterization using successive cancellation beamspace UCA algorithm," *IEEE Trans. Veh. Technol.*, vol. 68, no. 8, pp. 7248–7259, Aug. 2019.
[40] R. W. Heath, N. González-Prelcic, S. Rangan, W. Roh, and A. M. Sayeed, "An overview of signal processing techniques for millimeter wave MIMO systems," *IEEE J. Sel. Topics Signal Process.*, vol. 10, no. 3, pp. 436–453, Apr. 2016.
[41] F. Bowman, *Introduction to Bessel functions*. North Chelmsford, U.K.: Courier Corporation, 2012.
[42] Z. Wu, M. Cui, and L. Dai, "Enabling more users to benefit from near-field communications: From linear to circular array," *IEEE Trans. Wireless Commun.*, pp. 1–1, Sep. 2023.
[43] K. Spoof, V. Unnikrishnan, M. Zahra, K. Stadius, M. Kosunen, and J. Ryynänen, "True-time-delay beamforming receiver with RF resampling," *IEEE Trans. Circuits Syst.*, vol. 67, no. 12, pp. 4457–4469, Dec. 2020.
[44] A. M. Mathai and R. K. Saxena, *Generalized hypergeometric functions with applications in statistics and physical sciences*. Springer, 2006, vol. 348.
[45] A. Alkhateeb, G. Leus, and R. W. Heath, "Limited feedback hybrid precoding for multi-user millimeter wave systems," *IEEE Trans. Wireless Commun.*, vol. 14, no. 11, pp. 6481–6494, Jul. 2015.
[46] B. Ning, Z. Tian, W. Mei, Z. Chen, C. Han, S. Li, J. Yuan, and R. Zhang, "Beamforming technologies for ultra-massive MIMO in terahertz communications," *IEEE Open J. Commun. Soc.*, vol. 4, pp. 614–658, 2023.
[47] J. Mo, P. Schniter, and R. W. Heath, "Channel estimation in broadband millimeter wave MIMO systems with few-bit ADCs," *IEEE Trans. Signal Process.*, vol. 66, no. 5, pp. 1141–1154, Mar. 2018.
[48] Y. Chen, L. Yan, and C. Han, "Hybrid spherical- and planar-wave modeling and DCNN-powered estimation of terahertz ultra-massive MIMO channels," *IEEE Trans. Commun.*, vol. 69, no. 10, pp. 7063–7076, Oct. 2021.
[49] M. Abramowitz and I. A. Stegun, *Handbook of mathematical functions with formulas, graphs, and mathematical tables*. US Government printing office, 1948, vol. 55.

Zidong Wu received the B.E. degree in electronic engineering from Tsinghua University, Beijing, China, in 2019. He is currently pursuing the Ph.D. degree in Department of Electronic Engineering at Tsinghua University, Beijing, China. His research interests include massive MIMO, mmWave communications, and near-field communications. He has received the Honorary Mention of IEEE ComSoc Student Competition in 2019, IEEE ICC Oustanding Demo Award in 2022, and IEEE Best Paper Award at IEEE GLOBECOM 2023.

Linglong Dai (Fellow, IEEE) received the B.S. degree from Zhejiang University, Hangzhou, China, in 2003, the M.S. degree (with the highest honor) from the China Academy of Telecommunications Technology, Beijing, China, in 2006, and the Ph.D. degree (with the highest honor) from Tsinghua University, Beijing, China, in 2011. From 2011 to 2013, he was a Postdoctoral Research Fellow with the Department of Electronic Engineering, Tsinghua University, where he was an Assistant Professor from 2013 to 2016, an Associate Professor from 2016 to 2022, and has been a Professor since 2022. His current research interests include massive MIMO, reconfigurable intelligent surface (RIS), millimeter-wave and Terahertz communications, near-field communications, machine learning for wireless communications, and electromagnetic information theory.

He has coauthored the book *MmWave Massive MIMO: A Paradigm for 5G* (Academic Press, 2016). He has authored or coauthored over 100 IEEE journal papers and over 60 IEEE conference papers. He also holds over 20 granted patents. He has received five IEEE Best Paper Awards at the IEEE ICC 2013, the IEEE ICC 2014, the IEEE ICC 2017, the IEEE VTC 2017-Fall, the IEEE ICC 2018, and the IEEE GLOBECOM 2023. He has also received the Tsinghua University Outstanding Ph.D. Graduate Award in 2011, the Beijing Excellent Doctoral Dissertation Award in 2012, the China National Excellent Doctoral Dissertation Nomination Award in 2013, the URSI Young Scientist Award in 2014, the IEEE Transactions on Broadcasting Best Paper Award in 2015, the Electronics Letters Best Paper Award in 2016, the National Natural Science Foundation of China for Outstanding Young Scholars in 2017, the IEEE ComSoc Asia-Pacific Outstanding Young Researcher Award in 2017, the IEEE ComSoc Asia-Pacific Outstanding Paper Award in 2018, the China Communications Best Paper Award in 2019, the IEEE Access Best Multimedia Award in 2020, the IEEE Communications Society Leonard G. Abraham Prize in 2020, the IEEE ComSoc Stephen O. Rice Prize in 2022, the IEEE ICC Outstanding Demo Award in 2022, and the National Science Foundation for Distinguished Young Scholars in 2023. He was listed as a Highly Cited Researcher by Clarivate Analytics from 2020 to 2023. He was elevated as an IEEE Fellow in 2022.